J. Fluid Mech. (2013), *vol.* 723, *pp.* 352–373. © Cambridge University Press 2013
doi:10.1017/jfm.2013.128

Diffusion in hydrogel-supported phospholipid bilayer membranes

Chih-Ying Wang and Reghan J. Hill†

Department of Chemical Engineering, McGill University, Montreal, Quebec H3A 0C5, Canada

(Received 20 July 2012; revised 7 November 2012; accepted 26 February 2013;
first published online 16 April 2013)

We model a cylindrical inclusion (lipid or membrane protein) translating with velocity U in a thin planar membrane (phospholipid bilayer) that is supported above and below by Brinkman media (hydrogels). The total force F, membrane velocity, and solvent velocity are calculated as functions of three independent dimensionless parameters: $\Lambda = \eta a/(\eta_m h)$, ℓ_1/a and ℓ_2/a. Here, η and η_m are the solvent and membrane shear viscosities, a is the particle radius, h is the membrane thickness, and ℓ_1^2 and ℓ_2^2 are the upper and lower hydrogel permeabilities. As expected, the dimensionless mobility $4\pi\eta a U/F = 4\pi\eta a D/(k_B T)$ (proportional to the self-diffusion coefficient, D) decreases with decreasing gel permeabilities (increasing gel concentrations), furnishing a quantitative interpretation of how porous, gel-like supports hinder membrane dynamics. The model also provides a means of inferring hydrogel permeability and, perhaps, surface morphology from tracer diffusion measurements.

Key words: biological fluid dynamics, membranes, porous media

1. Introduction

This paper examines the fluid dynamics that accompany the translation of a molecular tracer embedded in a planar phospholipid bilayer membrane that is supported above and below by a porous, fluid-filled support, such as an hydrogel. Hydrogels are soft water-saturated polymer networks that have been studied extensively for tissue engineering and drug-delivery applications (Okano 1993; Hoare & Kohane 2008; Nicodemus & Bryant 2008). They have also been successful in supporting phospholipid bilayer membranes. In their natural state, phospholipid bilayers form the primary structure of the cell wall. Synthetic bilayers have novel applications in bio-sensing (Bayley & Cremer 2001) and drug-delivery applications (Sunamoto *et al.* 1987). When supported on hydrogels, they have been used for drug delivery (Kiser, Wilson & Needham 1998; An & Hubbell 2000; Ruel-Gariépy *et al.* 2002) and, more recently, to synthesize soft composites that change colour with mechanical stimulation (Haque *et al.* 2010).

Natural and synthetic membranes often include, to greatly varying extents, macromolecules and molecular assemblies, such as individual lipids (Batchelor *et al.* 2010; Alessandrini & Facci 2012), lipid rafts (Noble *et al.* 2009; Brameshuber *et al.* 2010; Orsini *et al.* 2012), and membrane proteins (Al-Abdul-Wahid *et al.* 2012; Zaitsev, Solovyeva & Nabiev 2012). The lateral mobility of these inclusions is critical

† Email address for correspondence: reghan.hill@mcgill.ca

https://doi.org/10.1017/jfm.2013.128 Published online by Cambridge University Press

to membrane function. In cell membranes, transmembrane proteins control signalling and the transport of nutrients and metabolites into and out of the cell (Farias *et al.* 2012). In technological applications, functionalization imparts unique properties for molecular sensing and sorting (Sackmann 1996; Sackmann & Tanaka 2000). For example, a transparent AlGaN-functionalized membrane system has furnished insights into the role of charge in the coupling of phospholipid bilayers to their support (Steinhoff *et al.* 2003).

Membrane tracer mobility has long been interpreted according to a continuum hydrodynamic model, first proposed by Saffman & Delbruck (1975), in which the tracer dimensions and membrane viscosity are the principal determinants of the lateral diffusion coefficient. However, it is well known that mobility is greatly reduced, or even completely arrested, when membranes are deposited onto hard supports (Evans & Sackmann 1988). Accordingly, polymer brushes (Zhao & Granick 2007) and fluid films (Castellana & Cremer 2006) have been adopted as spacers to help preserve membrane fluidity. Surprisingly, despite the extensive applications of hydrogels as bulk materials, little is known of how hydrogels perform as membrane supports.

Here, we propose an hydrogel-supported lipid bilayer model that quantifies the extent to which an hydrogel support hinders tracer (e.g. transmembrane protein) diffusion. This model also elucidates the nature of the membrane and hydrogel fluid velocity disturbances, which ultimately influence membrane mixing dynamics, and gradient and self-diffusion at finite tracer concentrations (see Bussell, Koch & Hammer 1994 and the references therein).

Saffman & Delbruck (1975) proposed the first hydrodynamic model of protein diffusion in freely supported bilayer membranes, furnishing an elegant formula that relates the Brownian diffusion coefficient to the tracer size, and membrane thickness and viscosity, when the forces are dominated by those from the membrane, i.e. when the dimensionless parameter

$$\Lambda = \eta a/(\eta_m h) \tag{1.1}$$

is much less than one. Here, η and η_m are the solvent and membrane shear viscosities, a is the tracer (disk) radius, and h is the membrane thickness. Note that the membrane viscosity is typically several orders of magnitude higher than that of water, so the net force is dominated by the two-dimensional membrane dynamics. Indeed, Saffman's seminal contribution here was to identify coupling of the membrane and support dynamics in the far field to resolve the Stokes paradox in which purely two-dimensional membrane velocity disturbances in an unbounded domain correspond to an indeterminate force (see Saffman 1976 for mathematical details).

Using analytical and numerical methodologies, Hughes, Pailthorpe & White (1981) extended the Saffman theory to arbitrary values of Λ, deriving a more accurate formula for $\Lambda \lesssim 1$ and identifying the limiting drag force for $\Lambda \gtrsim 1$. Evans & Sackmann (1988) addressed disc-shaped particles translating and rotating in membranes supported by a thin viscous sublayer. This model requires only solutions of the membrane equations of motion. Finally, Stone & Ajdari (1998) bridged the Saffman and Evans–Sackmann models, furnishing numerical solutions and analytical approximations for arbitrary sublayer thicknesses. They coupled the membrane and supporting fluid equations of motion using an ingenious integral-equation methodology, also providing an extensive analysis of the relevant length scales and their ordering in the extended parameter space.

We extend the methodology of Stone & Ajdari (1998) to Brinkman media, obtaining general solutions of Brinkman's equations above and below the membrane. By

https://doi.org/10.1017/jfm.2013.128 Published online by Cambridge University Press

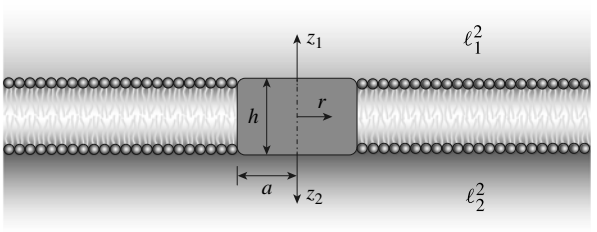


FIGURE 1. A planar phospholipid bilayer with membrane viscosity η_m and membrane thickness h bears a single, cylindrical inclusion (disk) with radius a. The membrane is supported above and below by hydrogels with permeabilities ℓ_1^2 and ℓ_2^2, both saturated by a solvent with shear viscosity η. The top and bottom solvent velocities equal the membrane velocity at the respective interfaces $z_1 = z_2 = 0$.

coupling the Brinkman fluid dynamics to the membrane dynamics, we compute the solvent and membrane velocities, membrane pressure, and the accompanying force arising from fluid and membrane stresses. As illustrated in figure 1, our model considers a lipid bilayer with thickness h and viscosity η_m that is supported above and below by Brinkman media with respective permeabilities ℓ_1^2 and ℓ_2^2. The translating particle, approximated as a disk with radius a and height h, represents a membrane inclusion (e.g. protein or lipid raft) that spans the bilayer thickness. Note, however, that this model may also apply to inclusions that span only half the membrane width, provided that lipids in the other leaflet bind tightly enough to the inclusion base.

For a particle translating with velocity U, $O(U\eta_m/a)$ membrane stresses furnish an $O(U\eta_m h)$ force. In a membrane supported by unbounded solvent, the solvent-phase viscous stresses are $O(U\eta/a)$, furnishing an $O(U\eta a)$ force. For rigid lipid assemblies, termed lipid rafts, the hydrodynamic radius can be up to 120 nm (Pike 2008), and the bilayer membrane viscosity varies with temperature and composition, often in the range $\eta_m \approx 1$–4 P (Fuchs *et al.* 1975) with the aqueous solvent viscosity $\eta \approx 0.01$ P $\ll \eta_m$. Using these ranges, the ratio of the foregoing solvent- and membrane-phase forces furnishes $\Lambda \approx 0.001$–1 for membranes with thickness $h \approx 1$–5 nm (Meyer *et al.* 1998).

For membranes supported by a Brinkman medium with $\ell \lesssim a$, the solvent-phase stress is $O(U\eta/\ell)$, because the velocity disturbance in a Brinkman medium decays on the length scale ℓ. Now, when the membrane-velocity disturbance decays on the same length scale (i.e. the solvent and membrane are tightly coupled with $\eta_m \ll \eta$) the membrane stress is $O(U\eta_m/\ell)$. Accordingly, the net force becomes $O[(1 + \Lambda^{-1})U\eta a^2/\ell]$ with $\Lambda > 1$, a scaling that we will verify from numerically exact calculations for arbitrary values of the independent dimensionless parameters.

Note that our model, like that of all the foregoing continuum hydrodynamic membrane models, assumes that the top and bottom leaflets are tightly coupled, so they both have the same membrane velocity $\boldsymbol{u}_m$. Moreover, the solvent above and below the membrane is assumed to satisfy a non-slip condition, furnishing $\boldsymbol{u}_1 = \boldsymbol{u}_2 = \boldsymbol{u}_m$ at $z_1 = z_2 = 0$. For integral monotopic proteins, which occupy only one leaflet, this model can be extended to permit slip between the top and bottom leaflets; the simplest model, perhaps, includes an interfacial stress, acting between the leaflets, that is proportional to the interfacial slip velocity, i.e. $\boldsymbol{\tau}_1 = -\gamma_{12}(\boldsymbol{u}_{m,1} - \boldsymbol{u}_{m,2})$, where γ_{12} is an inter-leaflet friction coefficient. Accordingly, the tightly coupled-leaflet

https://doi.org/10.1017/jfm.2013.128 Published online by Cambridge University Press

model explored in this work corresponds to $\gamma_{12} \to \infty$. We will examine the more general model in future work.

2. Theory

As shown in figure 1, the hydrodynamic model comprises two unbounded Brinkman half-spaces (e.g. hydrogels with Brinkman screening lengths ℓ_1 and ℓ_2, and solvent viscosity η) that support a flat lipid bilayer (membrane viscosity η_m and thickness h) in which a rigid cylindrical inclusion (lipid or protein with hydrodynamic radius a) is embedded and translates laterally (with velocity $\boldsymbol{U}$). The solvent velocity and pressure in the Brinkman media are governed by the momentum and mass conservation equations of Brinkman (1947),

$$-\boldsymbol{\nabla} p_i + \eta \nabla^2 \boldsymbol{u}_i - \frac{\eta}{\ell_i^2}\boldsymbol{u}_i = 0 \quad \text{and} \quad \boldsymbol{\nabla}\cdot\boldsymbol{u}_i = 0, \tag{2.1}$$

where $i = 1, 2$ identify the top and bottom half-spaces. The membrane velocity and pressure satisfy the Stokes equations

$$-\boldsymbol{\nabla} p_m + \eta_m \nabla^2 \boldsymbol{u}_m + \boldsymbol{f}_m = 0 \quad \text{and} \quad \boldsymbol{\nabla}\cdot\boldsymbol{u}_m = 0, \tag{2.2}$$

where

$$\boldsymbol{f}_m = \boldsymbol{f}_1 + \boldsymbol{f}_2 = \frac{1}{h}\boldsymbol{e}_z\cdot\boldsymbol{\sigma}_1 - \frac{1}{h}\boldsymbol{e}_z\cdot\boldsymbol{\sigma}_2 \quad (z_i = 0, r > a) \tag{2.3}$$

is a body force (per unit volume) from the shear stresses exerted by the solvent on the top and bottom surfaces: $\boldsymbol{e}_z$ is an upward unit vector, and $\boldsymbol{\sigma}_i = -p_i\boldsymbol{\delta} + \eta[\boldsymbol{\nabla}\boldsymbol{u}_i + (\boldsymbol{\nabla}\boldsymbol{u}_i)^{\mathrm{T}}]$ is the solvent stress tensor.

To justify neglecting the skeleton (i.e. hydrogel) deformation, we note that the hydrodynamic drag force exerted by the fluid on the skeleton is $O(\eta U/\ell^2)$ with $U = O(D/a)$, where D is the tracer diffusion coefficient. Therefore, balancing this hydrodynamic body force with an $O(\mu v_c/a^2)$ elastic stress (shear modulus μ) gives a characteristic skeleton displacement $v_c = O[\eta D a/(\mu\ell^2)]$. Thus, to achieve small $v_c \ll a$ requires $\eta D/(\mu\ell^2) \ll 1$, which can be interpreted as requiring the viscoelastic relaxation time η/μ to be short compared to a diffusion time ℓ^2/D. Next, we evoke the Stokes–Einstein relationship $D = k_B T/\gamma$ with a tracer friction coefficient $\gamma \gtrsim 4\pi\eta a$; the well-known relationships $\mu = k_B T n_e$, where n_e is the effective number density of active cross-links; and $\ell^{-2} = n_s 6\pi a_s$, where n_s is the number density of Stokes resistance centres with hydrodynamic radius a_s. Thus, we conclude that skeleton deformation may be neglected when the dimensionless parameter

$$\Pi = \frac{k_B T}{4\pi a \mu \ell^2} = \frac{3 n_s a_s}{2 n_e a} \ll 1. \tag{2.4}$$

As demonstrated below, this inequality can be satisfied for low-density agarose hydrogels, but not necessarily for all hydrogels and other hydrogel-like microstructures. For pressure-driven flow in supported agarose gel membranes, permeability measurements of Johnson & Deen (1996) furnish $\ell^2 \approx 0.0388\phi^{-2.46}\ \mathrm{nm}^2$ (at vanishing pressure gradient); here, the volume fraction $\phi \approx c/1.025$ and $0.02 \lesssim c \lesssim 0.07$ is the mass-to-volume fraction. Moreover, from ball-indentation experiments on thin agarose films, Ahearme *et al.* (2005) report Young's moduli E that furnish $E \approx 3\mu \approx 1.38c$ MPa when $0.004 \lesssim c \lesssim 0.01$. (Note that we have taken the Poisson ratio $\nu = 0.5$ in applying the more general identity $E = 2\mu(1+\nu)$.)

https://doi.org/10.1017/jfm.2013.128 Published online by Cambridge University Press

Thus, assuming these relationships can be extrapolated beyond the experimental range of agarose concentrations over which they were measured, we find $\Pi \approx 4.23 \times 10^{12} k_B T c^{1.46}/a \lesssim 1$ when $c \lesssim 0.14$ and $a = 1$ nm. Accordingly, agarose gels at the concentrations they are typically available ($0.003 \lesssim c \lesssim 0.1$) seem to be sufficiently stiff and permeable to prevent local deformation.

For polyacrylamide gels, however, matters are more complicated, because the permeability and rheological properties change with the total polymer concentration and the ratio of cross-linker (bis-acrylamide) to monomer units. For example, Yeung *et al.* (2005) synthesized gels with shear moduli in the range 0.01–50 kPa by varying the total polymer mass fraction from 3 % to 12 % with cross-linker ratios in the range 0.01–0.6 %. Note also that the cross-linking efficiency can decrease with increasing cross-linker ratio, producing a plateau in the shear modulus at cross-linker ratios greater than ∼3 % (Calvert, Wong & Giasson 2004). These influences also complicate the permeability relationship, sometimes producing a flow-rate-dependent permeability as evidence of flow-induced micro-structural deformation (Tokita & Tanaka 1991; Grattoni *et al.* 2001). Permeability measurements by Tokita & Tanaka (1991) with the cross-linker ratio fixed at 1 % furnish $\ell^2 \approx 0.0331 c^{-1.47}$ nm^2, where c is the total polymer mass fraction. Interestingly, Tokita & Tanaka (1991) found that increasing the cross-linker ratio actually increased the permeability, suggesting that spatial inhomogeneities are more influential on the permeability than the average degree of cross-linking. Extrapolating the shear moduli of Yeung *et al.* (2005) to a cross-linker ratio of 1 per cent with $c \approx 0.075$ furnishes $\mu \approx 30$ kPa. Therefore, with $\ell^2 \approx 1.2$ nm^2 (from Tokita & Tanaka), we find $\Pi \approx 7$. Accordingly, the balance of elastic and hydrodynamic friction forces in these gels may induce skeleton deformation. Even so, the degree to which such deformation might impact tracer diffusion may be weak if the deformation is dominated by shear modes; this is a matter for further investigation, which will not be further elaborated upon in this paper.

Note also that active skeleton dynamics (see Jülichera *et al.* 2007) may be relevant to tracer dynamics in natural lipid bilayers, but such dynamics are beyond the scope of the present study. Finally, we caution that the present model does not account for the tracer protruding beyond its bilayer into the supporting hydrogel. Nevertheless, there exist transmembrane proteins that have small protruding volumes (von Heijne 2007), e.g. acetylcholine receptor, subunit beta2, TMH 2 (2k59); calcium-gated potassium channel MthK (3ldc); and F1F0 ATP synthase (1c17) (Lomize *et al.* 2006). Clearly, future models should explore hydrodynamic and frictional coupling of more general tracers (including integral monotopic proteins) to the supporting skeleton.

Now returning to the model introduced above, the general solutions of Brinkman's equations (2.1),

$$u_{i,r}(r,\theta,z) = U\cos\theta \int_0^\infty [a_i(k)\mathrm{J}_0(kr) + b_i(k)\mathrm{J}_2(kr)]\exp[-\sqrt{k^2+\ell_i^{-2}}z_i] + kz_i\frac{a_i(k)-b_i(k)}{2\sqrt{k^2+\ell_i^{-2}}}[\mathrm{J}_2(kr)-\mathrm{J}_0(kr)]\,\mathrm{e}^{-kz_i}\,\mathrm{d}k, \tag{2.5}$$

$$u_{i,\theta}(r,\theta,z) = U\sin\theta \int_0^\infty [-a_i(k)\mathrm{J}_0(kr) + b_i(k)\mathrm{J}_2(kr)]\exp[-\sqrt{k^2+\ell_i^{-2}}z_i] + kz_i\frac{a_i(k)-b_i(k)}{2\sqrt{k^2+\ell_i^{-2}}}[\mathrm{J}_2(kr)+\mathrm{J}_0(kr)]\,\mathrm{e}^{-kz_i}\,\mathrm{d}k, \tag{2.6}$$

https://doi.org/10.1017/jfm.2013.128 Published online by Cambridge University Press

$$u_{i,z}(r,\theta,z) = U\cos\theta\int_0^\infty kz_i\frac{a_i(k)-b_i(k)}{\sqrt{k^2+\ell_i^{-2}}}\mathrm{J}_1(kr)\mathrm{e}^{-kz_i}\,\mathrm{d}k, \tag{2.7}$$

$$p_i(r,\theta,z) = 2\eta U\cos\theta\int_0^\infty k[a_i(k)-b_i(k)]\mathrm{J}_1(kr)\mathrm{e}^{-kz_i}\,\mathrm{d}k, \tag{2.8}$$

can be derived from the Hankel transform of (2.1) in a cylindrical coordinate system (see appendix A). Here, $\mathrm{J}_0(kr)$, $\mathrm{J}_1(kr)$, and $\mathrm{J}_2(kr)$ are Bessel functions of the first kind (see appendix D for identities used throughout this paper), and $a_i(k)$ and $b_i(k)$ are functions to be determined from the interfacial boundary conditions at $z_i = 0$. With the no-slip condition, setting $z_i = 0$ in the general solutions above furnishes the membrane velocity,

$$u_{m,r}(r,\theta,z) = U\cos\theta\int_0^\infty [a_m(k)\mathrm{J}_0(kr)+b_m(k)\mathrm{J}_2(kr)]\,\mathrm{d}k, \tag{2.9}$$

$$u_{m,\theta}(r,\theta,z) = U\sin\theta\int_0^\infty [-a_m(k)\mathrm{J}_0(kr)+b_m(k)\mathrm{J}_2(kr)]\,\mathrm{d}k. \tag{2.10}$$

Following Saffman (1976) and Hughes *et al.* (1981), the pressure and z-component of the velocity disturbances above and below a flat membrane are zero. Accordingly, $a_i(k) = b_i(k)$, giving

$$u_{i,r}(r,\theta,z) = U\cos\theta\int_0^\infty a_i(k)[\mathrm{J}_2(kr)+\mathrm{J}_0(kr)]\exp[-\sqrt{k^2+\ell_i^{-2}}z_i]\,\mathrm{d}k, \tag{2.11}$$

$$u_{i,\theta}(r,\theta,z) = U\sin\theta\int_0^\infty a_i(k)[\mathrm{J}_2(kr)-\mathrm{J}_0(kr)]\exp[-\sqrt{k^2+\ell_i^{-2}}z_i]\,\mathrm{d}k, \tag{2.12}$$

$$u_{m,r}(r,\theta) = U\cos\theta\int_0^\infty a_m(k)[\mathrm{J}_2(kr)+\mathrm{J}_0(kr)]\,\mathrm{d}k, \tag{2.13}$$

$$u_{m,\theta}(r,\theta) = U\sin\theta\int_0^\infty a_m(k)[\mathrm{J}_2(kr)-\mathrm{J}_0(kr)]\,\mathrm{d}k. \tag{2.14}$$

When the particle translates along the x-axis with velocity $\boldsymbol{U} = U\cos\theta\boldsymbol{e}_r - U\sin\theta\boldsymbol{e}_\theta$, the no-slip boundary condition at $z_i = 0$ demands

$$\int_0^\infty a_i(k)[\mathrm{J}_2(kr)+\mathrm{J}_0(kr)]\,\mathrm{d}k = 1 \quad (r\leqslant a), \tag{2.15}$$

which, using the identity $\mathrm{J}_2(kr)+\mathrm{J}_0(kr) = 2\mathrm{J}_1(kr)/(kr)$, can be written

$$2\int_0^\infty k^{-1}a_i(k)\mathrm{J}_1(kr)\,\mathrm{d}k = r \quad (r\leqslant a). \tag{2.16}$$

This condition, applied to the radial component of the velocity, also satisfies the tangential component because of the incompressibility constraint.

Next, taking the curl of (2.2) gives

$$\int_0^\infty ka\left[a_m(k)k^2a^2 + a_1(k)\Lambda\sqrt{(ka)^2+(a/\ell_1)^2}\right.$$
$$\left. + a_2(k)\Lambda\sqrt{(ka)^2+(a/\ell_2)^2}\right]\mathrm{J}_1(kr)\,\mathrm{d}k = 0 \quad (r>a), \tag{2.17}$$

where $\Lambda = \eta a/(\eta_m h)$ is a dimensionless parameter (see the Introduction) that compares the membrane and solvent forces on the inclusion. Finally, the membrane

https://doi.org/10.1017/jfm.2013.128 Published online by Cambridge University Press

pressure (see appendix B) is

$$p_m(r,\theta) = \frac{\eta_m U}{a}\cos\theta \int_0^\infty r\left[a_m(k)k^2 a + a_1(k)\Lambda\sqrt{k^2+\ell_1^{-2}} + a_2(k)\Lambda\sqrt{k^2+\ell_2^{-2}}\right][\mathrm{J}_2(kr)-\mathrm{J}_0(kr)]\,\mathrm{d}k, \tag{2.18}$$

and the net hydrodynamic force (see appendix C) is

$$\boldsymbol{F} = -\frac{2\pi\eta a\boldsymbol{U}}{\Lambda}\int\left[a_m(k)k^2a^2 + a_1(k)\Lambda a\sqrt{k^2+\ell_1^{-2}} + a_2(k)\Lambda a\sqrt{k^2+\ell_2^{-2}}\right]\mathrm{J}_2(ka)\,\mathrm{d}k. \tag{2.19}$$

3. Numerical solution

To solve (2.17) and (2.16) for $a_1(k) = a_2(k) = a_m(k)$, from which the solvent velocity, and the membrane velocity and pressure are constructed, we apply the direct numerical approach of Stone & Ajdari (1998), which draws on the works of Tranter (1966) and Tanzosh & Stone (1995). Stone & Ajdari addressed the problem of a translating disk in a membrane supported by an aqueous subphase with finite depth. They verified the methodology by comparing their results to analytical solutions of Saffman (1976), Hughes *et al.* (1981) and Evans & Sackmann (1988).

In this section, $a_i(k)$, k and r are dimensionless after scaling appropriately with a. Following Tranter (1966) and Sneddon (1966), it is convenient to let

$$a_i(k)k\left[k^2 + \Lambda_1\sqrt{k^2+(a/\ell_1)^2} + \Lambda_2\sqrt{k^2+(a/\ell_2)^2}\right] = k^{1-\beta}\sum_{n=0}^{\infty} a_{i,n}J_{2n+1+\beta}(k), \tag{3.1}$$

where $\beta > 0$ is an arbitrary constant that only affects the series convergence, and $a_{i,n}$ are constants that vary with the independent model parameters $\Lambda_1 = \Lambda_2 = \Lambda$, ℓ_1/a and ℓ_2/a. Note that (3.1) satisfies (2.17) (Sneddon 1966), so we need only seek $a_{i,n}$ to satisfy (2.16). Accordingly, substituting (3.1) into (2.16) gives

$$2\int_0^\infty \frac{k^{-1-\beta}\sum_{n=0}^{\infty} a_{i,n}J_{2n+1+\beta}(k)}{k^2+\Lambda\sqrt{k^2+(a/\ell_1)^2}+\Lambda\sqrt{k^2+(a/\ell_2)^2}}\mathrm{J}_1(kr)\,\mathrm{d}k = r \quad (r\leqslant 1). \tag{3.2}$$

Then, multiplying by

$$r^{1+\alpha}(1-r^2)^{\beta-1}\mathscr{J}_\nu(\alpha+\beta,\alpha+1,r^2), \tag{3.3}$$

where $\mathscr{J}_\nu$ are Jacobi polynomials, and integrating with respect to r from 0 to 1 gives

$$2\int_0^1 r^{1+\alpha}(1-r^2)^{\beta-1}\mathscr{J}_\nu(\alpha+\beta,\alpha+1,r^2) \times \int_0^\infty \frac{k^{-1-\beta}\sum_{n=0}^{\infty} a_{i,n}J_{2n+1+\beta}(k)\mathrm{J}_1(kr)}{k^2+\Lambda\sqrt{k^2+(a/\ell_1)^2}+\Lambda\sqrt{k^2+(a/\ell_2)^2}}\,\mathrm{d}k\,\mathrm{d}r = \int_0^1 r^{2+\alpha}(1-r^2)^{\beta-1}\mathscr{J}_\nu(\alpha+\beta,\alpha+1,r^2)\,\mathrm{d}r \quad (r\leqslant 1). \tag{3.4}$$

https://doi.org/10.1017/jfm.2013.128 Published online by Cambridge University Press

Next, applying the identities

$$\int_0^1 r^{1+2\alpha}\,(1-r^2)^{\beta-1}\,\mathscr{I}_\nu(\alpha+\beta,\alpha+1,r^2)\,\mathrm{d}r=\frac{\Gamma(1+\alpha)\Gamma(\beta)}{2\Gamma(\alpha+\beta+1)}\delta_{0\nu} \tag{3.5}$$

and

$$\int_0^1 r^{1+\alpha}\,(1-r^2)^{\beta-1}\,\mathscr{I}_\nu(\alpha+\beta,\alpha+1,r^2)J_\alpha(kr)\,\mathrm{d}r$$
$$=k^{-\beta}J_{\alpha+2\nu+\beta}(k)\frac{2^{\beta-1}\Gamma(\nu+\alpha)\Gamma(\nu+\beta)}{\Gamma(\alpha+\nu+1)}, \tag{3.6}$$

with $\alpha=1$ (Magnus, Oberhettinger & Soni 1966) (Γ is the Gamma function), we obtain

$$\sum_{n=0}^{\infty}a_{i,n}\int_0^\infty\frac{k^{-1-2\beta}J_{2n+1+\beta}(k)J_{2\nu+1+\beta}(k)}{k^2+\Lambda\sqrt{k^2+(a/\ell_1)^2}+\Lambda\sqrt{k^2+(a/\ell_2)^2}}\,\mathrm{d}k$$
$$=\frac{\Gamma(\nu+2)\Gamma(\beta)\delta_{0\nu}}{2^{\beta+1}\Gamma(\beta+2)\Gamma(\nu+\beta)}. \tag{3.7}$$

Thus, by letting $\nu=0,\,1,\,2,\ldots,N$, $a_{i,n}$ are furnished by truncating the sums to $n\leqslant N$ terms and evaluating the integrals using numerical quadrature.

Finally, applying the identity (Grandshteyn & Ryzhik 1965)

$$\int_0^\infty k^{-\beta}\mathrm{J}_2(k)J_{2n+1+\beta}(k)\,\mathrm{d}k=\frac{\delta_{0n}}{2^\beta\Gamma(2+\beta)}, \tag{3.8}$$

the force from (2.19) becomes

$$\boldsymbol{F}=-\frac{a_{i,0}\pi\eta a\boldsymbol{U}}{\Lambda 2^{\beta-1}\Gamma(2+\beta)}. \tag{3.9}$$

4. Results

All the computations reported here were executed with $\beta=0.0625$ and $N=12$ (Lucas 1995). These computational parameters achieved reasonable computational efficiency and economy, e.g. ensuring good agreement with the asymptotic limit $\Lambda\gg1$ with $\ell_1/a=\ell_2/a\gg1$ in which Hughes *et al.* (1981) showed that the dimensionless mobility $4\pi\eta aU/F\to\pi/4$. All computations were undertaken with a Matlab program, available from the corresponding author. With $N=12$, for example, a single force calculation requires $\approx$1.9 s of Matlab computation on a standard desktop computer.

We begin by examining how the dimensionless mobility $4\pi\eta aU/F$ depends on $\Lambda=\eta a/(\eta_m h)$ with $\ell_1/\ell_2=1$. We have chosen to plot the mobility rather than the resistance (or drag force) because this measure is proportional to the experimentally measured self-diffusion coefficient, D. From the Stokes–Einstein relationship, $D=k_BT/\gamma$, where the friction coefficient $\gamma\equiv F/U$. Accordingly, the dimensionless mobility $4\pi\eta aU/F=4\pi\eta aD/(k_BT)$ can be viewed as a dimensionless self-diffusion coefficient.

As shown in figure 2, this quantity for a bilayer supported by pure solvent ($\ell_1/a=\ell_2/a\to\infty$) increases from zero when $\Lambda\to0$ to an $O(1)$ plateau when $\Lambda\to\infty$. When $\Lambda\gg1$, the membrane stresses are simply $\sim\eta_mU/a$, giving a membrane drag force $\sim2\pi h\eta_mU$, whereas the stresses from the supporting solvent

https://doi.org/10.1017/jfm.2013.128 Published online by Cambridge University Press

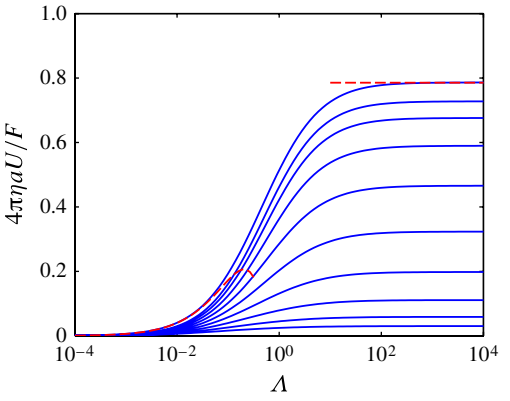


FIGURE 2. (Colour online) Scaled mobility (diffusion coefficient) $4\pi\eta aU/F$ versus $\Lambda = \eta a/(\eta_m h)$: $\ell_1/a = \ell_2/a = \infty$, 8, 4, 2, 1, 0.5, 0.25, 0.125, 0.125/2, 0.125/4 (top to bottom) (computations with $N = 12$). Dashed lines are the theories of Saffman (1976) ($\Lambda \ll 1$) and Hughes *et al.* (1981) ($\Lambda \gg 1$) for $\ell_1/a = \ell_2/a \to \infty$.

are $\sim\eta U/a$, giving a solvent drag force $\sim 8\pi a\eta U$. Thus, as $\Lambda \to \infty$, the total drag force appears to be dominated by the solvent drag, giving an $O(1)$ dimensionless mobility (Hughes *et al.* 1981),

$$4\pi\eta aU/F = \pi/4. \tag{4.1}$$

When $\Lambda \to 0$, our calculations agree with the asymptotic theory of Saffman (1976), which furnishes a dimensionless mobility

$$4\pi\eta aU/F \to \Lambda(\ln \Lambda^{-1} - \gamma) \ll 1, \tag{4.2}$$

where here $\gamma \approx 0.577$ is Euler's constant. Our results also agree with the computations of Hughes *et al.* (1981) for all intermediate values of Λ.

Figure 2 quantifies how the finite permeability of the supporting hydrogel skeletons hinder tracer diffusion. When $\ell_1/a = \ell_2/a = 1$, for example, the mobility is about half the value attained when supported by pure solvent. Similar results are shown in figure 3, but with asymmetric hydrogel configurations: $\ell_2/\ell_1 = 2$, 10 and 100. Breaking the symmetry does not change the qualitative form of the relationship shown with $\Lambda = 1$; it does, however, reduce the drag force and, thus, increase the mobility.

As $\ell_2/\ell_1 \to 0$ or ∞, the situation corresponds to a membrane supported by an hydrogel on one side and a pure solvent on the other. Carefully comparing the results in figures 2 and 3 confirms that the mobility for a singly supported membrane (i.e. $\ell_2/\ell_1 = 100$) is indeed higher than for a doubly supported membrane (figure 2) with the same hydrogel permeability. Note also that the difference between the singly and doubly supported cases increases with decreasing hydrogel permeability. When $\ell_1/a \lesssim 1$, for example, the hydrogel contribution to the stress is $\sim\eta U/\ell_1$, giving a force $\sim 4\pi a^2\eta U/\ell_1$. Thus, with two supporting hydrogels, the drag force is $\sim 4\pi a^2\eta U(\ell_1^{-1} + \ell_2^{-1})$, giving a dimensionless mobility $4\pi\eta aU/F \sim 1/(a/\ell_1 + a/\ell_2)$ when $a/\ell_1 + a/\ell_2 \gg 1$.

Evans & Sackmann (1988) derived a mobility formula for disks in membranes supported on one side by a thin layer of Newtonian fluid (via a membrane-support friction coefficient), neglecting stresses on the other side. Generalizing their formula for membranes supported on both sides by thin layers of Newtonian fluid (having the

https://doi.org/10.1017/jfm.2013.128 Published online by Cambridge University Press

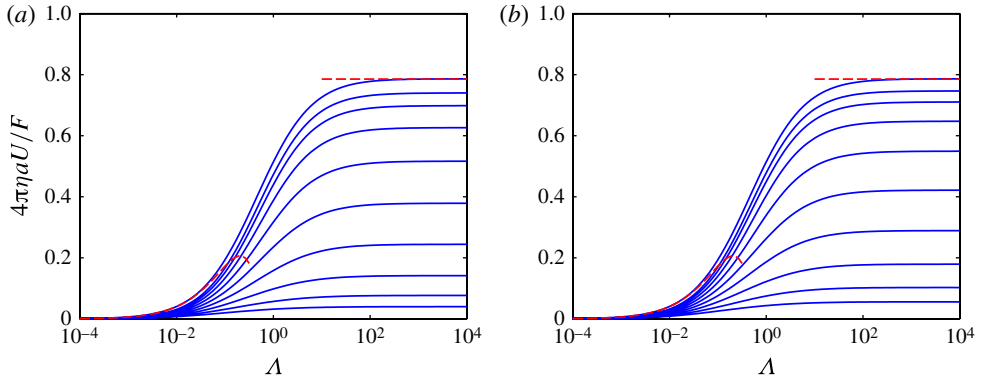


FIGURE 3. (Colour online) Same as figure 2, but with (*a*) $\ell_2/\ell_1 = 2$ and (*b*) 100.

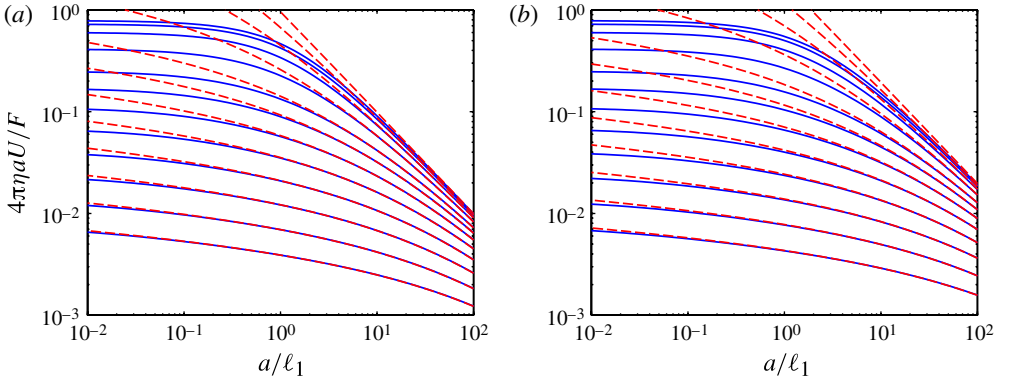


FIGURE 4. (Colour online) Scaled mobility (diffusion coefficient) $4\pi\eta aU/F$ versus a/ℓ_1: (*a*) $\ell_2/\ell_1 = 1$ and (*b*) 100; $\Lambda = 0.0025/2, 0.0025, 0.005, 0.01, 0.02, 0.04, 0.08, 0.16, 0.5, 2, 10, 1000$ (bottom to top) (computations with $N = 12$). Dashed lines are the theory of Evans & Sackmann (1988) (equation (4.3)) evaluated with $\epsilon^2 = \Lambda(a/\ell_1 + a/\ell_2)$.

same viscosity η) with thicknesses set to ℓ_1 and ℓ_2 furnishes

$$4\pi\eta aU/F = \Lambda\,[\epsilon^2/2 + \epsilon \mathrm{K}_1(\epsilon)/\mathrm{K}_0(\epsilon)]^{-1}, \tag{4.3}$$

where $\epsilon^2 = \Lambda(a/\ell_1 + a/\ell_2)$, and $\mathrm{K}_0(\epsilon)$ and $\mathrm{K}_1(\epsilon)$ are modified Bessel functions of the second kind. (Note that setting the layer thicknesses to ℓ_1 and ℓ_2 above is motivated by considering the hydrodynamic slip length for simple shear flow past a Brinkman medium with permeability ℓ^2: with a continuous velocity and shear stress at the interface, the velocity disturbance in the Brinkman medium decays exponentially fast with a decay length ℓ.) Equation (4.3) is compared with our exact calculations in figure 4, here with logarithmically scaled mobility axes and two values of $\ell_2/\ell_1 = 1$ (figure 4*a*) and 100 (figure 4*b*). As expected, excellent agreement is obtained when $\Lambda \gg 1$ with $a/\ell_1, a/\ell_2 \gg 1$. Note that, when $\ell_2 \gg \ell_1$, the exact calculations include viscous stresses on both sides of the membrane, whereas the Evans–Sackmann theory is appropriate only when ℓ_1 and ℓ_2 are sufficiently small (see Stone & Ajdari 1998 for an extensive analysis of the relevant length scales and their ordering).

https://doi.org/10.1017/jfm.2013.128 Published online by Cambridge University Press

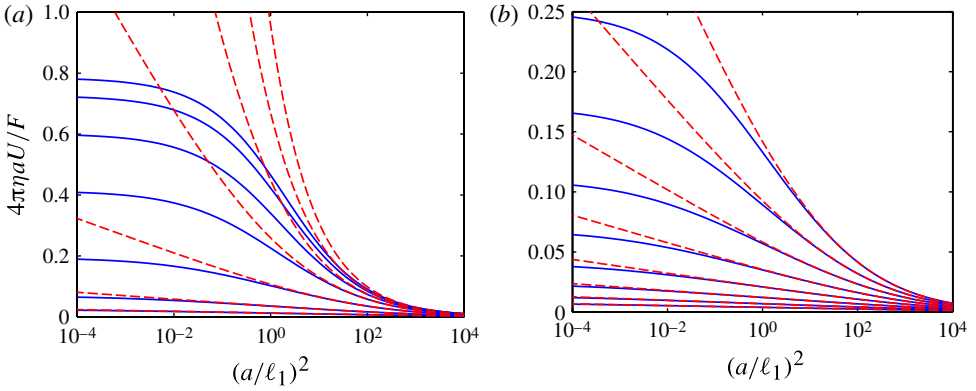


FIGURE 5. (Colour online) Scaled mobility (diffusion coefficient) $4\pi\eta aU/F$ versus $(a/\ell_1)^2$: $\ell_2/\ell_1 = 1$: (*a*) $\Lambda = 0.005$, 0.02, 0.1, 0.5, 2, 10, 1000 (bottom to top); (*b*) $\Lambda = 0.0025/2$, 0.0025, 0.005, 0.01, 0.02, 0.04, 0.08, 0.16 (bottom to top) (computations with $N = 12$). Dashed lines are the theory of Evans & Sackmann (1988) (equation (4.3)) evaluated with $\epsilon^2 = \Lambda(a/\ell_1 + a/\ell_2)$.

In practice, membrane diffusion experiments will be undertaken with systematic variations in the hydrogel permeability, achieved by varying the pre-monomer concentration and cross-linking density. If an hydrogel is modelled as a uniform distribution of Stokes resistance centres, with number density n and hydrodynamic radius a_h, then the permeability $\ell_i^2 = 1/(n_i 6\pi\eta a_h)$. Accordingly, to show more directly how increasing the hydrogel concentration or density might affect the diffusion coefficient, figure 5 shows the scaled mobility $4\pi\eta aU/F$ versus $(a/\ell_1)^2 = a^2 n 6\pi\eta a_h$ with various values of Λ. In this manner, the mobility is more clearly demonstrated to decrease with increasing hydrogel concentration. Figure 5(*b*) expands the mobility axis for $\Lambda \ll 1$. Note that the qualitative form of the relationship is the same as for larger Λ. Fitting experimental data to the model, to infer the hydrogel permeability, for example, will require careful determination of the underlying dimensional parameters.

Next, we examine the membrane velocity disturbances, as furnished by the membrane velocity streamlines (see appendix E). The streamlines for membranes supported above and below by the same hydrogel ($\ell_2/\ell_1 = 1$) are shown in figures 6–8 for three representative values of Λ. Flows with $\ell_2/\ell_1 = 100$, mimicking singly supported membranes (not shown), are qualitatively very similar. The most striking qualitative features of the disturbances, compared to membranes supported by pure solvent ($\ell_1/a = \ell_2/a \gg 1$, figures 6*d*, 7*d* and 8*d*), are recirculation regions. These prevail under conditions where the dominant forces acting on the tracer are from the shear stresses acting on the top and bottom surfaces, i.e. when $\ell_1/a = \ell_2/a \lesssim 1$ or $\Lambda \gtrsim 1$. Similarly to porous-media flows, the membrane disturbances are screened by their hydrodynamic coupling to the hydrogel, in a very similar manner to a thin fluid subphase (Evans & Sackmann 1988).

Radial and tangential membrane velocities are shown in figure 9 with $\Lambda = 1$ and $\ell_1/a = \ell_2/a = 0.1$, 1, 10 and 100. Similar plots with $\Lambda = 0.01$ and 100 are available in appendix F. The radial velocity, plotted as a function of distance along the polar axis ($\theta = 0$), decays as r^{-2} when $r - a \gtrsim \ell_1 = \ell_2$. In figure 10, the radial solvent ($\theta = 0$) velocity is plotted as a function of distance along the z_1-axis, again with $\Lambda = 1$ and $\ell_1/a = \ell_2/a = 0.1$, 1, 10 and 100. Similar plots with $\Lambda = 0.01$ and 100 are available in appendix F. As expected, when $\ell_1/a = \ell_2/a \lesssim 1$, the velocity disturbance decays exponentially fast with a characteristic decay length ℓ_1. However,

https://doi.org/10.1017/jfm.2013.128 Published online by Cambridge University Press

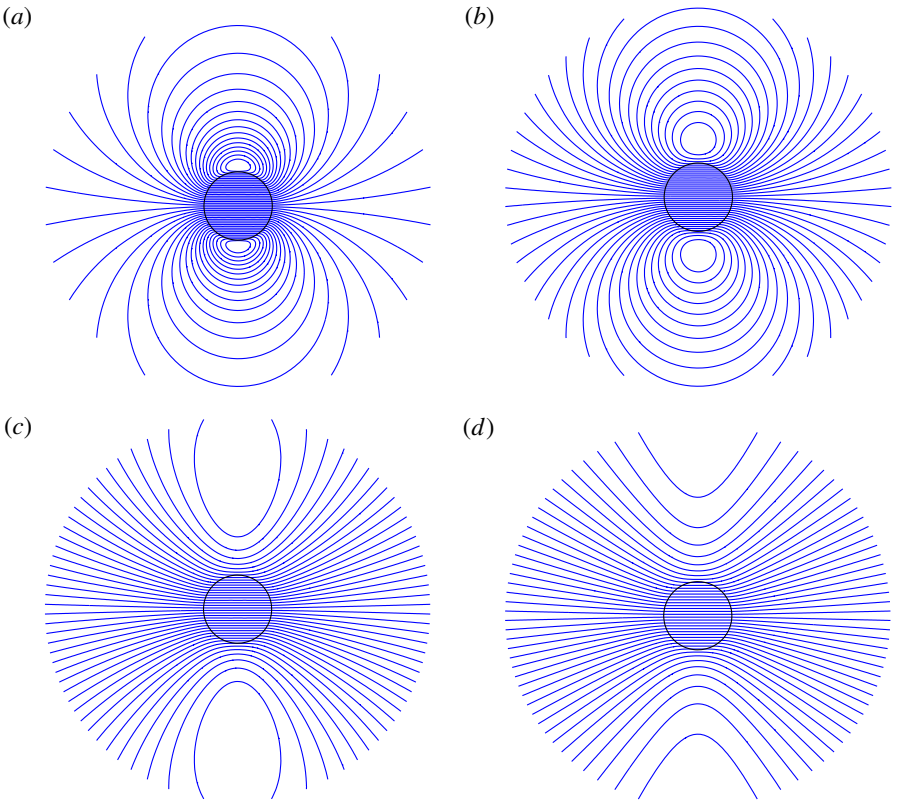


FIGURE 6. (Colour online) Membrane streamlines with $\Lambda = 1$: (*a*) $\ell_1/a = \ell_2/a = 0.1$, (*b*) 1, (*c*) 10, (*d*) 100 (computations with $N = 12$).

when $\ell_1/a = \ell_2/a \gtrsim 1$, the disturbance decays on the length scale a/Λ, because the fluid dynamics are dominated by the membrane.

5. Conclusions

We have extended models of tracer diffusion in phospholipid membranes by coupling the membrane hydrodynamics to Brinkman flows on each side of a flat membrane. This model furnishes the drag coefficient, mobility, and single-particle self-diffusion coefficient of a compact, cylindrical inclusion, such as a transmembrane protein or a lipid raft, in a membrane that is supported on each side by rigid porous skeletons, e.g. synthetic hydrogels, cytoskeletons, or biofilms. As expected, the porous supports hinder tracer diffusion because of the increased rate of viscous dissipation. Transverse membrane disturbances penetrate each porous medium by a distance that is equal to the respective Brinkman screening length (square root of the Darcy permeability). The porous supports also screen lateral membrane disturbances, producing short-ranged recirculating flow when the Brinkman screening length is comparable to or smaller than the tracer. Finally, we caution that the present model does not allow for a thin lubricating layer of solvent between the membrane and porous media (important when the thickness of such a layer is smaller than the Brinkman screening length); neither does it account for slip between bilayer

https://doi.org/10.1017/jfm.2013.128 Published online by Cambridge University Press

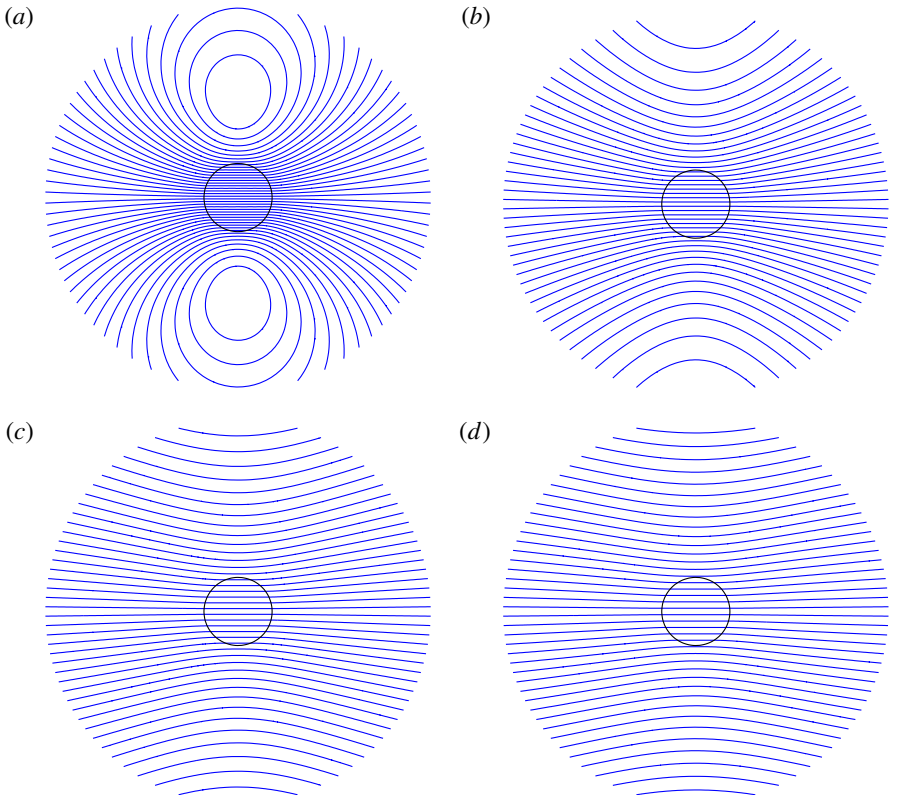


FIGURE 7. (Colour online) Same as figure 6, but with $\Lambda = 0.01$.

leaflets, or penetration of the tracer beyond the membrane. Nevertheless, it does furnish an important and necessary step toward quantitative interpretations of tracer diffusion coefficients in hydrogel-supported lipid bilayer membranes. We are at present measuring tracer diffusion coefficients in various hydrogel-supported synthetic bilayers, finding that the diffusion coefficient decreases monotonically with increasing hydrogel concentration, as predicted by the theory. These data and quantitative comparisons with theory will be reported elsewhere.

Acknowledgements

R.J.H. gratefully acknowledges support from the Natural Sciences and Engineering Research Council of Canada (NSERC) and the Canada Research Chairs program. C.-Y.W. thanks the Faculty of Engineering, McGill University, for support through a McGill Engineering Doctoral Award (MEDA).

Appendix A. Hankel transform of Brinkman's equations

Following Saffman (1976), writing Brinkman's equations in cylindrical coordinates (r, θ, z) gives

$$\frac{1}{\eta}\frac{\partial p}{\partial r} = \frac{\partial}{\partial r}\left[\frac{1}{r}\frac{\partial}{\partial r}(ru_r)\right] + \frac{1}{r^2}\frac{\partial^2 u_r}{\partial \theta^2} - \frac{2}{r^2}\frac{\partial u_\theta}{\partial \theta} + \frac{\partial^2 u_r}{\partial z^2} - \frac{1}{\ell^2}u_r, \tag{A 1}$$

https://doi.org/10.1017/jfm.2013.128 Published online by Cambridge University Press

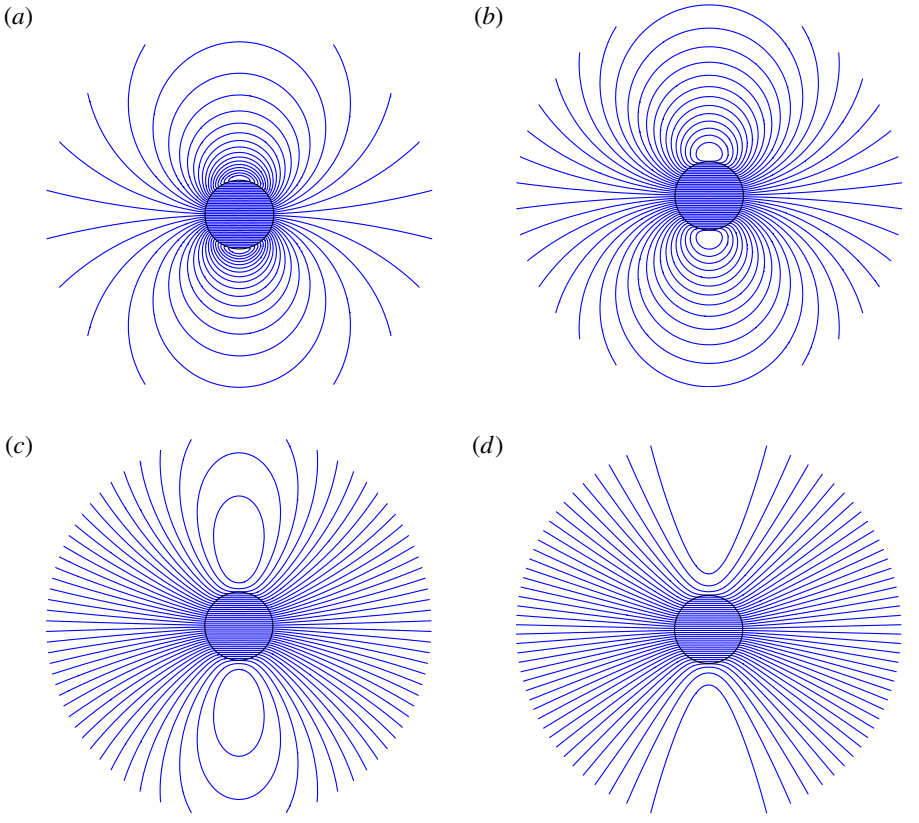


FIGURE 8. (Colour online) Same as figure 6, but with $\Lambda = 100$.

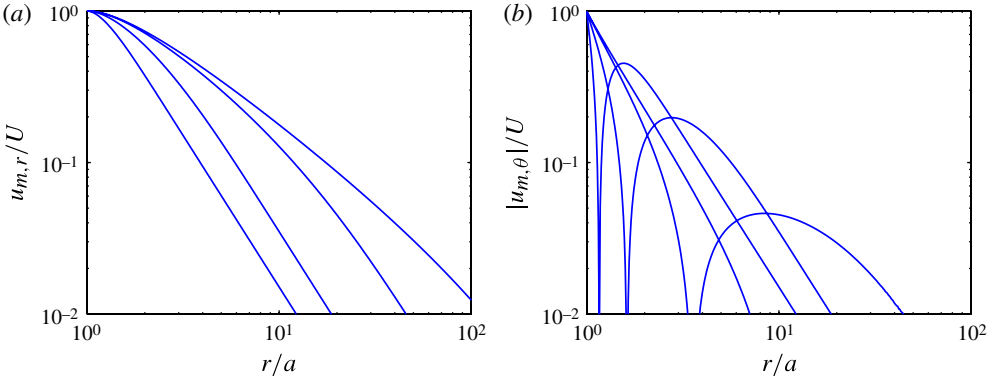


FIGURE 9. (Colour online) (*a*) Radial ($\theta = 0$), and (*b*) tangential ($\theta = \pi/2$), membrane velocity profiles: $\Lambda = 1$; $\ell_1/a = \ell_2/a = 0.1$, 1, 10, 100 (left to right) (computations with $N = 12$).

https://doi.org/10.1017/jfm.2013.128 Published online by Cambridge University Press

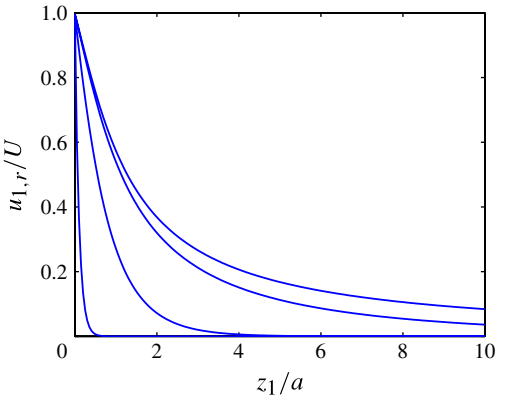


FIGURE 10. (Colour online) Radial solvent velocity profiles ($r = 0, \theta = 0$): $\Lambda = 1$; $\ell_1/a = \ell_2/a = 0.1$ (bottom), 1, 10, 100 (top) (computations with $N = 12$).

$$\frac{1}{\eta}\frac{1}{r}\frac{\partial p}{\partial \theta} = \frac{\partial}{\partial r}\left[\frac{1}{r}\frac{\partial}{\partial r}(ru_\theta)\right] + \frac{1}{r^2}\frac{\partial^2 u_\theta}{\partial \theta^2} + \frac{2}{r^2}\frac{\partial u_r}{\partial \theta} + \frac{\partial^2 u_\theta}{\partial z^2} - \frac{1}{\ell^2}u_\theta, \tag{A 2}$$

$$\frac{1}{\eta}\frac{\partial p}{\partial z} = \frac{1}{r}\frac{\partial}{\partial r}\left(r\frac{\partial u_z}{\partial r}\right) + \frac{1}{r^2}\frac{\partial^2 u_z}{\partial \theta^2} + \frac{\partial^2 u_r}{\partial z^2} - \frac{1}{\ell^2}u_z, \tag{A 3}$$

with continuity equation

$$\frac{1}{r}\frac{\partial}{\partial r}(ru_r) + \frac{1}{r}\frac{\partial u_\theta}{\partial \theta} + \frac{\partial u_z}{\partial z} = 0. \tag{A 4}$$

Next, writing the velocity and pressure as

$$u_r(r, \theta, z) = \bar{u}_r(r, z)\cos\theta, \tag{A 5a}$$

$$u_\theta(r, \theta, z) = \bar{u}_\theta(r, z)\sin\theta, \tag{A 5b}$$

$$u_z(r, \theta, z) = \bar{u}_z(r, z)\cos\theta, \tag{A 5c}$$

$$p(r, \theta, z) = \eta\bar{p}(r, z)\cos\theta, \tag{A 5d}$$

gives

$$\frac{\partial \bar{p}}{\partial r} = \frac{\partial}{\partial r}\left[\frac{1}{r}\frac{\partial}{\partial r}(r\bar{u}_r)\right] - \frac{1}{r^2}\bar{u}_r - \frac{2}{r^2}\bar{u}_\theta + \frac{\partial^2 \bar{u}_r}{\partial z^2} - \frac{1}{\ell^2}\bar{u}_r, \tag{A 6}$$

$$-\frac{1}{r}\bar{p} = \frac{\partial}{\partial r}\left[\frac{1}{r}\frac{\partial}{\partial r}(r\bar{u}_\theta)\right] - \frac{1}{r^2}\bar{u}_\theta - \frac{2}{r^2}\bar{u}_\theta + \frac{\partial^2 \bar{u}_\theta}{\partial z^2} - \frac{1}{\ell^2}\bar{u}_\theta, \tag{A 7}$$

$$\frac{\partial \bar{p}}{\partial z} = \frac{1}{r}\frac{\partial}{\partial r}\left(r\frac{\partial \bar{u}_z}{\partial r}\right) - \frac{1}{r^2}\frac{\partial^2 \bar{u}_z}{\partial \theta^2} + \frac{\partial^2 \bar{u}_z}{\partial z^2} - \frac{1}{\ell^2}\bar{u}_z, \tag{A 8}$$

$$0 = \frac{1}{r}\frac{\partial}{\partial r}(r\bar{u}_r) + \frac{1}{r}\bar{u}_\theta + \frac{\partial \bar{u}_z}{\partial z}. \tag{A 9}$$

Adding and subtracting the radial and tangential equations gives

$$r\frac{\partial}{\partial r}\left(\frac{\bar{p}}{r}\right) = \left(\frac{\partial^2}{\partial r^2} + \frac{1}{r}\frac{\partial}{\partial r} - \frac{4}{r^2}\right)(\bar{u}_r + \bar{u}_\theta) + \frac{\partial^2}{\partial z^2}(\bar{u}_r + \bar{u}_\theta) - \frac{1}{\ell^2}(\bar{u}_r + \bar{u}_\theta), \tag{A 10}$$

https://doi.org/10.1017/jfm.2013.128 Published online by Cambridge University Press

$$\frac{1}{r}\frac{\partial}{\partial r}(r\bar{p}) = \left(\frac{\partial^2}{\partial r^2} + \frac{1}{r}\frac{\partial}{\partial r}\right)(\bar{u}_r - \bar{u}_\theta) + \frac{\partial^2}{\partial z^2}(\bar{u}_r - \bar{u}_\theta) - \frac{1}{\ell^2}(\bar{u}_r - \bar{u}_\theta). \quad (A\,11)$$

Now, seeking solutions of the form

$$\bar{u}_r(r,z) = \int_0^\infty [A(k,z)\mathrm{J}_0(kr) + B(k,z)\mathrm{J}_2(kr)]\,\mathrm{d}k, \quad (A\,12a)$$

$$\bar{u}_\theta(r,z) = \int_0^\infty [C(k,z)\mathrm{J}_0(kr) + D(k,z)\mathrm{J}_2(kr)]\,\mathrm{d}k, \quad (A\,12b)$$

$$\bar{u}_z(r,z) = \int_0^\infty U_z(k,z)k\mathrm{J}_1(kr)\,\mathrm{d}k, \quad (A\,12c)$$

$$\bar{p}(r,z) = \int_0^\infty P(k,z)k\mathrm{J}_1(kr)\,\mathrm{d}k, \quad (A\,12d)$$

where the coefficients A, B, C, D, U_z and P must satisfy

$$\frac{\partial P}{\partial z} = \left(-k^2 + \frac{\partial^2}{\partial z^2} - \frac{1}{\ell^2}\right)U_z, \quad (A\,13)$$

$$-A + B + \frac{\partial U_z}{\partial z} = 0, \quad (A\,14)$$

$$-k^2 P = \left(-k^2 + \frac{\partial^2}{\partial z^2} - \frac{1}{\ell^2}\right)(B + D), \quad (A\,15)$$

$$k^2 P = \left(-k^2 + \frac{\partial^2}{\partial z^2} - \frac{1}{\ell^2}\right)(A - C), \quad (A\,16)$$

with $A = -C$ and $B = D$, gives

$$u_r(r,\theta,z) = U\cos\theta \int_0^\infty [a(k)\mathrm{J}_0(kr) + b(k)\mathrm{J}_2(kr)]\exp[-\sqrt{k^2+\ell^{-2}}z] + kz\frac{a(k)-b(k)}{2\sqrt{k^2+\ell^{-2}}}[\mathrm{J}_2(kr) - \mathrm{J}_0(kr)]\mathrm{e}^{-kz}\,\mathrm{d}k, \quad (A\,17)$$

$$u_\theta(r,\theta,z) = U\sin\theta \int_0^\infty [-a(k)\mathrm{J}_0(kr) + b(k)\mathrm{J}_2(kr)]\exp[-\sqrt{k^2+\ell^{-2}}z] + kz\frac{a(k)-b(k)}{2\sqrt{k^2+\ell^{-2}}}[\mathrm{J}_2(kr) + \mathrm{J}_0(kr)]\mathrm{e}^{-kz}\,\mathrm{d}k, \quad (A\,18)$$

$$u_z(r,\theta,z) = U\cos\theta \int_0^\infty kz\frac{a(k)-b(k)}{\sqrt{k^2+\ell^{-2}}}\mathrm{J}_1(kr)\mathrm{e}^{-kz}\,\mathrm{d}k, \quad (A\,19)$$

$$p(r,\theta,z) = 2\eta U\cos\theta \int_0^\infty k[a(k) - b(k)]\mathrm{J}_1(kr)\mathrm{e}^{-kz}\,\mathrm{d}k. \quad (A\,20)$$

Appendix B. Membrane pressure

The membrane momentum conservation equation gives

$$\boldsymbol{\nabla} p_m = \eta_m \nabla^2 \boldsymbol{u}_m + \boldsymbol{f}_m, \quad (B\,1)$$

https://doi.org/10.1017/jfm.2013.128 Published online by Cambridge University Press

so substituting the membrane velocity and body force from the main text gives

$$\begin{aligned}\nabla p_m &= \eta_m\left[\frac{1}{r}\frac{\partial}{\partial r}\left(r\frac{\partial u_{mr}}{\partial r}\right)+\frac{1}{r^2}\frac{\partial^2 u_{mr}}{\partial\theta^2}-\frac{u_{mr}}{r^2}-\frac{2}{r^2}\frac{\partial u_{m\theta}}{\partial\theta}\right]\boldsymbol{e}_r\\ &+\eta_m\left[\frac{1}{r}\frac{\partial}{\partial r}\left(r\frac{\partial u_{m\theta}}{\partial r}\right)+\frac{1}{r^2}\frac{\partial^2 u_{m\theta}}{\partial\theta^2}-\frac{u_{m\theta}}{r^2}+\frac{2}{r^2}\frac{\partial u_{mr}}{\partial\theta}\right]\boldsymbol{e}_\theta\\ &-\frac{\eta U\cos\theta}{h}\sqrt{k^2+\ell_1^{-2}}\int_0^\infty a_1(k)[\mathrm{J}_2(kr)+\mathrm{J}_0(kr)]\,\mathrm{d}k\boldsymbol{e}_r\\ &-\frac{\eta U\sin\theta}{h}\sqrt{k^2+\ell_1^{-2}}\int_0^\infty a_1(k)[\mathrm{J}_2(kr)-\mathrm{J}_0(kr)]\,\mathrm{d}k\boldsymbol{e}_\theta\\ &-\frac{\eta U\cos\theta}{h}\sqrt{k^2+\ell_2^{-2}}\int_0^\infty a_2(k)[\mathrm{J}_2(kr)+\mathrm{J}_0(kr)]\,\mathrm{d}k\boldsymbol{e}_r\\ &-\frac{\eta U\sin\theta}{h}\sqrt{k^2+\ell_2^{-2}}\int_0^\infty a_2(k)[\mathrm{J}_2(kr)-\mathrm{J}_0(kr)]\,\mathrm{d}k\boldsymbol{e}_\theta. \end{aligned}\tag{B 2}$$

Integrating with respect to θ at fixed r, or with respect to r at fixed θ, gives

$$\begin{aligned}p_m(r,\theta) &= \frac{\eta_m U}{a}\cos\theta\int_0^\infty r\left[a_m(k)k^2a+a_1(k)\Lambda\sqrt{k^2+\ell_1^{-2}}\right.\\ &\left.+\ a_2(k)\Lambda\sqrt{k^2+\ \ell_2^{-2}}\right][\mathrm{J}_2(kr)-\mathrm{J}_0(kr)]\,\mathrm{d}k. \end{aligned}\tag{B 3}$$

Appendix C. Force

The total hydrodynamic force has contributions from the solvent traction acting on the top and bottom surfaces (each with area πa^2), and the membrane traction acting on the disk wall (area $2\pi ah$):

$$\boldsymbol{F}=\boldsymbol{F}_m+\boldsymbol{F}_1+\boldsymbol{F}_2,\tag{C 1}$$

where

$$\boldsymbol{F}_m=\int_{A_m}\boldsymbol{\sigma}_m\cdot\boldsymbol{e}_r\,\mathrm{d}A_m,\quad \boldsymbol{F}_1=\int_{A_1}\boldsymbol{\sigma}_1\cdot\boldsymbol{e}_z\,\mathrm{d}A_1\quad\text{and}\quad \boldsymbol{F}_2=-\int_{A_2}\boldsymbol{\sigma}_2\cdot\boldsymbol{e}_z\,\mathrm{d}A_2.\tag{C 2}$$

Symmetry and linearity with respect to $\boldsymbol{U}$ give

$$\boldsymbol{F}_m=\int_{A_m}\boldsymbol{e}_x\cdot\boldsymbol{\sigma}_m\cdot\boldsymbol{e}_r\,\mathrm{d}A_m\boldsymbol{e}_x\quad\text{and}\quad \boldsymbol{F}_1+\boldsymbol{F}_2=\int_{A_1}\boldsymbol{e}_x\cdot(\boldsymbol{\sigma}_1-\boldsymbol{\sigma}_2)\cdot\boldsymbol{e}_z\,\mathrm{d}A_1\boldsymbol{e}_x,\tag{C 3}$$

where $\boldsymbol{e}_x=\cos\theta\boldsymbol{e}_r-\sin\theta\boldsymbol{e}_\theta$, $\mathrm{d}A_m=ha\,\mathrm{d}\theta$, and $\mathrm{d}A_1=r\,\mathrm{d}r\,\mathrm{d}\theta$. Accordingly.

$$\boldsymbol{F}_m=ha\int_0^{2\pi}(\sigma_{m,rr}\cos\theta-\sigma_{m,\theta r}\sin\theta)\,\mathrm{d}\theta\boldsymbol{e}_x\tag{C 4}$$

and

$$\begin{aligned}\boldsymbol{F}_1+\boldsymbol{F}_2 &= \int_0^{2\pi}\int_0^a(\sigma_{1,rz}\cos\theta-\sigma_{1,\theta z}\sin\theta)r\,\mathrm{d}r\,\mathrm{d}\theta\boldsymbol{e}_x\\ &-\int_0^{2\pi}\int_0^a(\sigma_{2,rz}\cos\theta-\sigma_{2,\theta z}\sin\theta)r\,\mathrm{d}r\,\mathrm{d}\theta\boldsymbol{e}_x, \end{aligned}\tag{C 5}$$

https://doi.org/10.1017/jfm.2013.128 Published online by Cambridge University Press

where

$$\sigma_{m,rr} = -p_m + 2\eta_m \frac{\partial u_{m,r}}{\partial r}$$
$$= -p_m - \eta_m U \cos\theta \int_0^\infty a_m(k) \frac{4}{r} \mathrm{J}_2(kr)\, \mathrm{d}k, \tag{C 6}$$
$$\sigma_{m,\theta r} = \eta_m \left[\frac{1}{r} \frac{\partial u_{m,r}}{\partial \theta} + r \frac{\partial}{\partial r} \left(\frac{u_{m,\theta}}{r} \right) \right]$$
$$= \eta_m U \sin\theta \int_0^\infty a_m(k) \left[2k\mathrm{J}_1(kr) - \frac{4}{r} \mathrm{J}_2(kr) \right] \mathrm{d}k, \tag{C 7}$$

and

$$\sigma_{i,rz} = \eta \left(\frac{\partial u_r}{\partial z} + \frac{\partial u_z}{\partial r} \right)$$
$$= -\eta U \cos\theta \int_0^\infty a_i(k) \sqrt{k^2 + \ell_i^{-2}} [\mathrm{J}_2(kr) + \mathrm{J}_0(kr)] \exp[-\sqrt{k^2 + \ell_i^{-2}} z]\, \mathrm{d}k, \tag{C 8}$$
$$\sigma_{i,\theta z} = \eta \left(\frac{\partial u_\theta}{\partial z} + \frac{1}{r} \frac{\partial u_z}{\partial \theta} \right)$$
$$= -\eta U \sin\theta \int_0^\infty a_i(k) \sqrt{k^2 + \ell_i^{-2}} [\mathrm{J}_2(kr) - \mathrm{J}_0(kr)] \exp[-\sqrt{k^2 + \ell_i^{-2}} z]\, \mathrm{d}k. \tag{C 9}$$

Finally, evaluating the integrals gives

$$\boldsymbol{F}_m = -\pi\eta a \boldsymbol{U} \int a \left[a_1(k) \sqrt{k^2 + \ell_1^{-2}} + a_2(k) \sqrt{k^2 + \ell_2^{-2}} \right] [\mathrm{J}_2(ka) - \mathrm{J}_0(ka)]\, \mathrm{d}k$$
$$- \pi\eta a \boldsymbol{U} \Lambda^{-1} \int a_m(k) \{ 2ka\mathrm{J}_1(ka) + k^2 a^2 [\mathrm{J}_2(ka) - \mathrm{J}_0(ka)] \}\, \mathrm{d}k \tag{C 10}$$

and

$$\boldsymbol{F}_1 + \boldsymbol{F}_2 = -\pi\eta a \boldsymbol{U} \int_0^\infty a_1(k) a \sqrt{k^2 + \ell_1^{-2}}\, [\mathrm{J}_2(kr) + \mathrm{J}_0(kr)]\, \mathrm{d}k$$
$$- \pi\eta a \boldsymbol{U} \int_0^\infty a_2(k) a \sqrt{k^2 + \ell_2^{-2}}\, [\mathrm{J}_2(kr) + \mathrm{J}_0(kr)]\, \mathrm{d}k. \tag{C 11}$$

Note that we have used the identity $\mathrm{J}_1(ka) = 0.5ka[\mathrm{J}_2(ka) + \mathrm{J}_0(ka)]$.

Appendix D. Useful identities

The following equations are used repeatedly in the main text and appendices. From Grandshteyn & Ryzhik (1965),

$$J_{-\alpha}(kr) = (-1)^\alpha J_\alpha(kr), \tag{D 1}$$
$$\frac{2\alpha}{kr} J_\alpha(kr) = J_{\alpha-1}(kr) + J_{\alpha+1}(kr), \tag{D 2}$$

with orthogonality relation

$$\int_0^\infty J_\alpha(s) J_\beta(s) \frac{\mathrm{d}s}{s} = \frac{2}{\pi} \frac{\sin\left[\frac{\pi}{2}(\alpha - \beta)\right]}{\alpha^2 - \beta^2}. \tag{D 3}$$

https://doi.org/10.1017/jfm.2013.128 Published online by Cambridge University Press

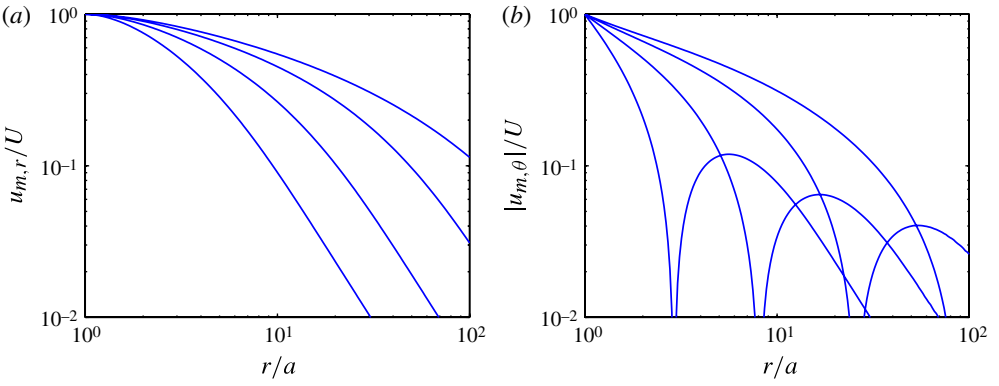


FIGURE 11. (Colour online) Same as figure 9 in the main text but with $\Lambda = 0.01$.

Also, Bourget's hypothesis (Hildebrand 1956) for $\alpha - 1$ dependence gives

$$\frac{\mathrm{d}}{\mathrm{d}r}J_\alpha(kr) = kJ_{\alpha-1}(kr) - \frac{\alpha}{r}J_\alpha(kr), \tag{D 4}$$

and $\alpha + 1$ dependence

$$\frac{\mathrm{d}}{\mathrm{d}r}J_\alpha(kr) = -kJ_{\alpha+1}(kr) + \frac{\alpha}{r}J_\alpha(kr). \tag{D 5}$$

Appendix E. Streamline computation

For the two-dimensional membrane flow, the stream function is (here, r and k are scaled appropriately with a)

$$\psi(r,\theta) = \int u_{m,r} r\,\mathrm{d}\theta = -\int u_{m,\theta}\,\mathrm{d}r. \tag{E 1}$$

When considering the form of the membrane velocity, it is computationally more efficient to integrate the radial component, giving

$$\psi(r,\theta) = \int u_{m,\theta} r\,\mathrm{d}\theta = Ur\sin\theta \int_0^\infty a_m(k)[\mathrm{J}_2(kr) + \mathrm{J}_0(kr)]\,\mathrm{d}k, \tag{E 2}$$

where

$$a_m(k) \approx \frac{k^{-\beta}\displaystyle\sum_{n=0}^{N} a_{i,n}J_{2n+1+\beta}(k)}{k^2 + \Lambda\sqrt{k^2 + (a/\ell_1)^2} + \Lambda\sqrt{k^2 + (a/\ell_2)^2}}. \tag{E 3}$$

Appendix F. Supplementary figures

Radial and tangential membrane velocities were shown in figure 9 with $\Lambda = 1$ and $\ell_1/a = \ell_2/a = 0.1$, 1, 10 and 100 in the main text. Similar plots with $\Lambda = 0.01$ and 100 are shown in this appendix in figures 11 and 12. Also, in the main text in figure 10, the radial solvent ($\theta = 0$) velocity was plotted as a function of distance along the z_1-axis, again with $\Lambda = 1$ and $\ell_1/a = \ell_2/a = 0.1$, 1, 10 and 100. Similar plots with $\Lambda = 0.01$ and 100 are shown in this appendix in figures 13 and 14.

https://doi.org/10.1017/jfm.2013.128 Published online by Cambridge University Press

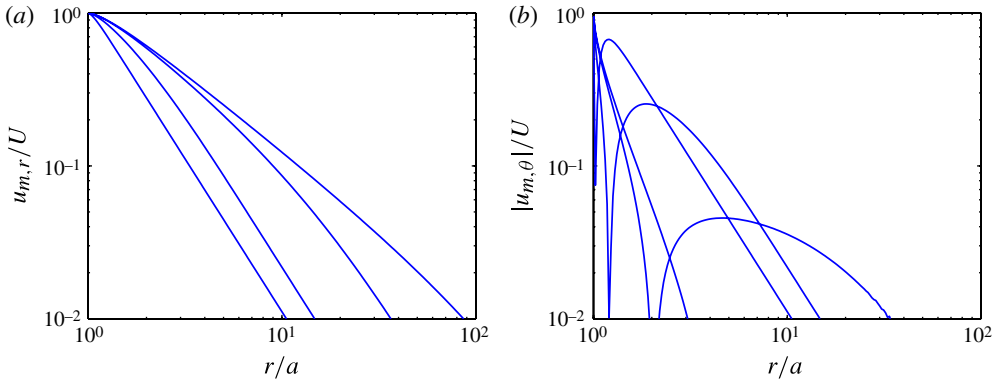


FIGURE 12. (Colour online) Same as figure 9 in the main text but with $\Lambda = 100$.

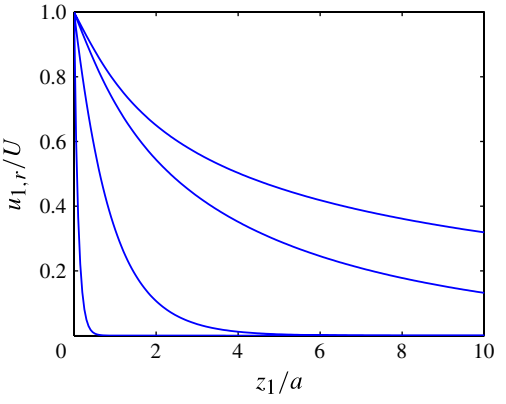


FIGURE 13. (Colour online) Same as figure 10 in the main text but with $\Lambda = 0.01$.

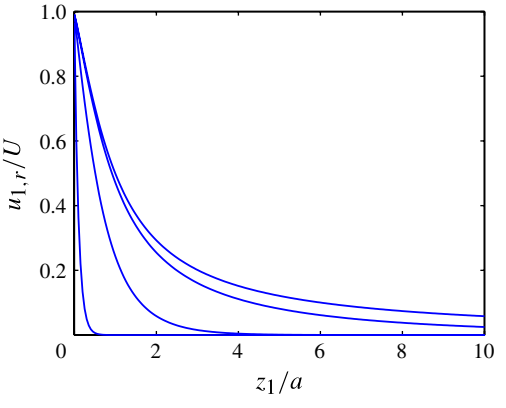


FIGURE 14. (Colour online) Same as figure 10 in the main text but with $\Lambda = 100$.

https://doi.org/10.1017/jfm.2013.128 Published online by Cambridge University Press

REFERENCES

AHEARME, M., YANG, Y., HAJ, A. J. E., THEN, K. Y. & LIU, K.-K. 2005 Characterizing the viscoelastic properties of thin hydrogel-based constructs for tissue engineering applications. *J. R. Soc. Interface* **2** (5), 455–463.

AL-ABDUL-WAHID, M. S., DEMILL, C. M., SERWIN, M. B., PROSSER, R. S. & STEWART, B. A. 2012 Effect of juxtamembrane tryptophans on the immersion depth of synaptobrevin, an integral vesicle membrane protein. *Biochim. Biophys. Acta* **1818**, 2994–2999.

ALESSANDRINI, A. & FACCI, P. 2012 Nanoscale mechanical properties of lipid bilayers and their relevance in biomembrane organization and function. *Micron* **43**, 1212–1223.

AN, Y. & HUBBELL, J. A. 2000 Intraarterial protein delivery via intimally-adherent bilayer hydrogels. *J. Control. Release* **64**, 205–215.

BATCHELOR, R., WINDLE, C. J., BUCHOUX, S. & LORCH, M. 2010 Cholesterol and lipid phases influence the interactions between serotonin receptor agonists and lipid bilayers. *J. Biol. Chem.* **285**, 41402–41411.

BAYLEY, H. & CREMER, P. S. 2001 Stochastic sensors inspired by biology. *Nature* **413**, 226–230.

BRAMESHUBER, M., WEGHUBER, J., RUPRECHT, V., GOMBOS, I., HORVATH, I., VIGH, L., ECKERSTORFER, P., KISS, E., STOCKINGER, H. & SCHUTZ, G. J. 2010 Imaging of mobile long-lived nanoplatforms in the live cell plasma membrane. *J. Biol. Chem.* **285**, 41765–41771.

BRINKMAN, H. C. 1947 A calculation of the viscous force exerted by a flowing fluid on a dense swarm of particles. *Appl. Sci. Res.* A **1**, 27–34.

BUSSELL, S. J., KOCH, D. L. & HAMMER, D. A. 1994 The effect of hydrodynamic interactions on the tracer and gradient diffusion of integral membrane proteins in lipid bilayers. *J. Fluid Mech.* **258**, 167–190.

CALVERT, D., WONG, J. Y. & GIASSON, S. 2004 Rheological monitoring of polyacrylamide gelation: importance of cross-link density and temperature. *Macromolecules* **37**, 7762–7771.

CASTELLANA, E. T. & CREMER, P. S. 2006 Solid supported lipid bilayers: from biophysical studies to sensor design. *Surf. Sci. Rep.* **61**, 429–444.

EVANS, E. & SACKMANN, E. 1988 Translational and rotational drag coefficients for a disk moving in a liquid membrane associated with a rigid substrate. *J. Fluid Mech.* **194**, 553–561.

FARIAS, G. G., CUITINO, L., GUO, X., REN, X., JARNIK, M., MATTERA, R. & BONIFACINO, J. S. 2012 Signal-mediated, ap-1/clathrin-dependent sorting of transmembrane receptors to the somatodendritic domain of hippocampal neurons. *Neuron* **75**, 810–823.

FUCHS, P., PAROLA, A., ROBBINS, P. W. & BLOUT, E. R. 1975 Fluorescence polarization and viscosity of membrane lipids 3t3 cells. *Proc. Natl Acad. Sci. USA* **72**, 3351–3354.

GRANDSHTEYN, I. S. & RYZHIK, I. M. 1965 *Tables of Integrals, Series and Products*. Academic.

GRATTONI, C. A., AL-SHARJI, H. H., YANG, C., MUGGERIDGE, A. H. & ZIMMERMAN, R. W. 2001 Rheology and permeability of corsslinked polyacrylamide gel. *J. Colloid Interface Sci.* **240**, 601–607.

HAQUE, M. A., KAMITA, G., KUROKAWA, T., TSUJII, K. & GONG, J. P. 2010 Unidirectional alignment of lamellar bilayer in hydrogel: one-dimensional swelling, anisotropic modulus, and stress/strain tunable structural color. *Adv. Mater.* **22**, 5110–5114.

VON HEIJNE, G. 2007 Membrane-protein topology. *Nature Rev. Mol. Cell Biol.* **7**, 910–918.

HILDEBRAND, F. B. 1956 *Advanced Calculus for Engineers*. Prentice Hall.

HOARE, T. R. & KOHANE, D. S. 2008 Hydrogels in drug delivery: progress and challenges. *Polymer* **49**, 1993–2007.

HUGHES, B. D., PAILTHORPE, B. A. & WHITE, L. R. 1981 The translational and rotational drag on a cylinder moving in a membrane. *J. Fluid Mech.* **110**, 349–372.

JOHNSON, E. M. & DEEN, W. M. 1996 Hydraulic permeability of agarose gels. *AIChE J.* **42**, 1220–1224.

JÜLICHERA, R., KRUSEA, K., PROST, J. & JOANNY, J.-F. 2007 Active behavior of the cytoskeleton. *Phys. Rep.* **449**, 3–28.

KISER, P. F., WILSON, G & NEEDHAM, D. 1998 A synthetic mimic of the secretory granule for drug delivery. *Nature* **394**, 459–462.

https://doi.org/10.1017/jfm.2013.128 Published online by Cambridge University Press

LOMIZE, M. A., LOMIZE, A. L., POGOZHEVA, I. D. & MOSBERG, H. I. 2006 OPM: orientations of proteins in membranes database. *Bioinformatics* **22** (5), 623–625.

LUCAS, S. K. 1995 Evaluating infinite integrals involving products of Bessel functions of arbitrary order. *J. Comput. Appl. Maths* **64**, 269–282.

MAGNUS, W., OBERHETTINGER, F. & SONI, R. P. 1966 *Formulas and Theorems for the Special Functions of Mathematical Physics*. Springer.

MEYER, H. W., WESTERMANN, M., STUMPF, M., RICHTER, W., ULRICH, A. S. & HOISCHEN, C. 1998 Minimal radius of curvature of lipid bilayers in the gel phase state corresponds to the dimension of biomembrane structures'caveolae'. *J. Struct. Biol.* **124**, 77–87.

NICODEMUS, G. D. & BRYANT, S. J. 2008 Cell encapsulation in biodegradable hydrogels for tissue engineering applications. *Tissue Engng B - Rev.* **14**, 149–165.

NOBLE, G. T., FLITSCH, S. L., LIEM, K. P. & WEBB, S. J. 2009 Assessing the cluster glycoside effect during the binding of concanavalin a to mannosylated artificial lipid rafts. *Org. Biomol. Chem.* **7**, 5245–5254.

OKANO, T. 1993 Molecular design of temperature-responsive polymers as intelligent materials. *Adv. Polym. Sci.* **110**, 179–197.

ORSINI, F., CREMONA, A., AROSIO, P., CORSETTO, P. A., MONTORFANO, G., LASCIALFARI, A. & RIZZO, A. M. 2012 Atomic force microscopy imaging of lipid rafts of human breast cancer cells. *Biochim. Biophys. Acta* **1818**, 2943–2949.

PIKE, L. J. 2008 The challenge of lipid rafts. *J. Lipid Res.* **50**, 323–328.

RUEL-GARIÉPY, E., LECLAIR, G., HILDGEN, P., GUPTA, A. & LEROUX, J.-C. 2002 T hermosensitive chitosan-based hydrogel containing liposomes for the delivery of hydrophilic molecules. *J. Control. Release* **82**, 373–383.

SACKMANN, E. 1996 Supported membranes: scientific and practical applications. *Science* **271**, 43–48.

SACKMANN, E. & TANAKA, M. 2000 Supported membranes on soft polymer cushions: fabrication, characterization and applications. *Trends Biotechnol.* **18**, 58–64.

SAFFMAN, P. G. 1976 Brownian motion in thin sheets of viscous fluid. *J. Fluid Mech.* **73**, 593–602.

SAFFMAN, P. G. & DELBRUCK, M. 1975 Brownian motion in biological membranes. *Proc. Natl Acad. Sci. USA* **72**, 3111–3113.

SNEDDON, I. N. 1966 *Mixed Boundary Value Problems in Potential Theory*. John Wiley & Sons.

STEINHOFF, G., PURRUCKER, O., TANAKA, M., STUTZMANN, M. & EICKHOFF, M. 2003 $Al_xGa_{1-x}N$-A new material system for biosensors. *Adv. Funct. Mater.* **13** (11), 841–846.

STONE, H. A. & AJDARI, A. 1998 Hydrodynamics of particles embedded in a flat surfactant layer overlying a subphase of finite depth. *J. Fluid Mech.* **369**, 151–173.

SUNAMOTO, J., SATO, T., HIROTA, M., FUKUSHIMA, K., HIRATANI, K. & HARA, K. 1987 A newly developed immunoliposome – an egg phosphatidylcholine liposome coated with pullulan bearing both a cholesterol moiety and an IgMs fragment. *Biochim. Biophys. Acta* **898**, 323–330.

TANZOSH, J. P. & STONE, H. A. 1995 Transverse motion of a disk through a rotating viscous fluid. *J. Fluid Mech.* **301**, 295–324.

TOKITA, M. & TANAKA, T. 1991 Friction coefficient of polymer networks of gels. *J. Chem. Phys.* **95** (6), 4613–4619.

TRANTER, C. J. 1966 *Integral Transforms in Mathematical Physics*. John Wiley & Sons.

YEUNG, T., GEORGES, P. C., FLANAGAN, L. A., MARG, B., ORTIZ, M., FUNAKI, M., NASTARAN, Z., MING, W., WEAVER, V. & JANMEY, P. A. 2005 Effects of substrate stiffness on cell morphology, cytoskeletal structure, and adhesion. *Cell Motil. Cytoskel.* **60**, 24–34.

ZAITSEV, S. Y., SOLOVYEVA, D. O. & NABIEV, I. 2012 Thin films and assemblies of photosensitive membrane proteins and colloidal nanocrystals for engineering of hybrid materials with advanced properties. *Adv. Colloid Interface Sci.* **183–184**, 14–29.

ZHAO, J. & GRANICK, S. 2007 How polymer surface diffusion depends on surface coverage. *Macromolecules* **40**, 1243–1247.

https://doi.org/10.1017/jfm.2013.128 Published online by Cambridge University Press